Characterising the response of vegetation cover to water limitation in Africa using geostationary satellites

Çağlar Küçük [1,2], Sujan Koirala [1], Nuno Carvalhais [1,3], Diego G. Miralles [2], Markus Reichstein [1], Martin Jung [1]

[1]Department of Biogeochemical Integration, Max Planck Institute for Biogeochemistry, Jena, Germany
[2]Hydro-Climate Extremes Lab (H-CEL), Faculty of Bioscience Engineering, Ghent University, Ghent, Belgium
[3]CENSE, Departamento de Ciências e Engenharia do Ambiente, Faculdade de Ciências e Tecnologia, Universidade NOVA de Lisboa, Caparica, Portugal

Key Points:

- We provide observation based metrics from FVC time series over Africa, characterising the dynamics of vegetation during water limitation
- The metrics, derived from daily FVC data with 0.0417°, have strong diagnostic power to understand fine-scale vegetation–water interactions
- Focused on water-limited periods, the metrics can be used to test hypothesis and constrain models on highly uncertain processes

Corresponding author: Çağlar Küçük, ckucuk@bgc-jena.mpg.de

Abstract

Plant available water is a key driver of ecosystem processes in water-limited systems. The interactions between vegetation, soil moisture, groundwater, and lateral redistribution of moisture in landscapes are complex and very heterogeneous. This complexity, together with the scarcity of relevant observations, creates a major obstacle for large-scale ecohydrological analysis and modelling. Here we exploit recent advancements in remote sensing at high spatial and temporal resolutions to extract relevant information on ecohydrological functioning. Our approach focuses on characterising vegetation dynamics along the seasonal wet to dry season transition, i.e. with progressive water limitation.

We present a set of observation-based metrics to characterise ecohydrological patterns across Africa at 0.0417° spatial resolution. These are derived from the daily time series of Fraction of Vegetation Cover (FVC) over the period 2004–2019 from the geostationary satellite Meteosat Second Generation. The metrics include (i) minimum and maximum FVC, (ii) start day, duration, and FVC integral of the dry season, and (iii) the decay rate of FVC during dry-down. The metrics reflect the potential state, temporal extent, and evolution of the limiting factors of FVC, which, in Africa, are predominantly associated with water availability. They provide information on the relevance of secondary moisture sources such as ground water access or ecohydrological buffering due to deep rooting. Analysis of the metrics reveals large-scale gradients with aridity, as well as regional patterns associated with topographic moisture variations. Our observation-based products have large potential for better understanding and modelling the complex vegetation-water interactions from regional to continental scales.

Plain Language Summary

Despite their importance on global carbon and water cycles, together with the ecosystem services, local-scale processes controlling vegetation dynamics under water-limitation are highly uncertain in large scale studies. This is particularly important in Africa due to the scarcity of ground measurements and stronger dependency of population on ecosystem services. In order to overcome this problem, we developed a set of metrics based on the fractional vegetation cover observed from the European geostationary satellite with daily temporal resolution. The metrics are suitable to diagnose local-scale processes thanks to their high spatial resolution of $\sim$ 5 km. First analyses show consistent continental gradients in the metrics together with strong local variations and corroboration with different datasets from independent sources.

1 Introduction

Africa hosts the largest share of undernourished population, and livelihood of the majority of population relies on ecosystem services, ecosystem productivity and water availability (Müller et al., 2014). African ecosystems contribute strongly to variations in the global carbon cycle (Williams et al., 2007; Valentini et al., 2014; Palmer et al., 2019; Weber et al., 2009), in which large uncertainties remain due to limited observations to model complex ecohydrological interactions happening with a wide spectrum over Africa. Most of the ecosystems in Africa are clearly controlled by water availability not only in arid and semiarid regions, but also in tropical forest in Central Africa (Zhou et al., 2014; Guan et al., 2015). Therefore, understanding the vegetation–water interactions in Africa is crucial.

Vegetation access to water is driven by rainfall but modulated by the interplay among hillslope topography (Fan et al., 2019), soil properties, groundwater (Maxwell & Condon, 2016), and root traits (Maeght et al., 2013). Meanwhile ecosystem properties controlling water use are likely adapted to climate and local hydrological conditions (Gentine et al., 2012). Representation of such complex and fine-scale interactions between vegetation, soil moisture, and groundwater within diverse landscapes still poses a challenge for land surface modellers (Clark et al., 2015; Fisher & Koven, 2020), and is hampered by the scarcity of observational constraints, especially for Africa.

Analysis of remotely-sensed vegetation indices provides opportunities to infer controlling environmental factors and land surface characteristics over large spatial domains. As most of the ecosystems in Africa are subject to moisture limitations, patterns of vegetation indices from remote sensing retrievals can be a proxy of underlying ecohydrological processes. In addition, annual recurrence of distinct wet and dry seasons over Africa provides a natural test bed to infer the effects of progressive water limitation and secondary water resources.

Characterising vegetation dynamics during dry season transition is challenging. Classical phenological metrics (reviewed in Zeng et al., 2020), such as the start and the end of the growing season, developed from the perspective of energy limited ecosystems. However, they are not tailored to the particularities of water-limited systems, i.e., vegetation with the ability to access secondary water resources in hillslope scales. In contrast to temperature or radiation, soil moisture has a strong memory with a gradual decline of water over the dry season. Besides, the end of growing season varies with vegetation properties, e.g., rooting depth, and moisture storage capacity depending on climate, soil and topographic characteristics. As such, characteristics of vegetation dry-down reflects the underlying ecohydrological processes and the limiting factors.

In this study, we characterise the dynamics of vegetation in the water-limiting period, i.e., the dry season, instead of those in the growing season. Here, the dry season is defined as the time period from the start of the effects of water limitations on vegetation cover, i.e., the peak of growing season, to the end of water limitation, i.e., the onset of the next growing season (see Fig. 1). The definition takes a vegetation perspective and complements the more traditional approaches using atmospheric forcing like precipitation thresholds. Furthermore, distinct temporal features of vegetation dynamics in the dry season provide indications of ecohydrological properties directly relevant to vegetation, such as ecosystem water storage capacity, access to secondary water resources due to groundwater or topographic moisture convergence, and ecosystem water use efficiency during photosynthesis. Undoubtedly, mapping such ecohydrological characteristics in space facilitates a better understanding, and subsequent modelling of vegetation–water interactions. We are aware that many factors influence temporal dynamics of vegetation cover and that the potential attribution to ecohydrological phenomena is contingent on the presence of predominately water-limited ecosystems such as over most of Africa.

We provide a set of relevant ecohydrological metrics for the African continent at $\sim 0.04^\circ$ spatial resolution. As mentioned previously, these metrics were derived using the vegetation dynamics in the decay phase in the time series. It should here be noted that the vegetation decay in Africa is mostly associated with water availability. Throughout this manuscript, we, therefore, use decay interchangeably with dry season, and associate both of them with vegetation dynamics under water limitation. The ecohydrological metrics were derived from the daily Fraction of Vegetation Cover (FVC) from geostationary satellite observations (see Sec. 2). The set of derived metrics (illustrated in Fig. 1) encompasses:

1. the asymptotic values for minimum and maximum of the FVC,
2. start day and duration of the dry season and the integral of FVC in the dry season, and
3. the exponential decay rate of FVC during dry-down.

The spatial patterns in minimum FVC, hereafter FVC_{min}, are likely related to the minimum amount of plant available water that would support vegetation activity via secondary water resources, i.e., deeper soil moisture and/or groundwater. The maximum FVC may be indicative of the maximum plant accessible water; and together with FVC_{min} allows for assessing the seasonal changes in vegetation (associated with water limitation). Since the cumulative water stress is expected to shape plant adaptation to prevailing water conditions (Caylor et al., 2009; Good & Caylor, 2011), the identification of the start and duration of the dry season is fundamental for ecohydrology. The integral of FVC over the dry season essentially diagnoses the total vegetation activity during the dry season, and is thus indicative of the vegetations dry season water consumption. The integral can be used to diagnose ecosystems' buffering capacity for progressive water limitation during dry season, say, due to deep root distribution.

The time scale of FVC decay is estimated for dry-down events, i.e., when ecosystems are predominantly water-limited. To do so, we assume that the plant available water is a single-pool linear storage reservoir with an exponential decline over time. Such assumption has been previously applied to satellite retrievals of surface soil moisture, showing associations of the decay with soil texture and aridity (McColl et al., 2017). Similarly, the e-folding time of evapotranspiration observed from eddy covariance flux towers revealed patterns of associations with plant height and seasonal aridity (Teuling et al., 2006; Boese et al., 2019; Martínez-de la Torre et al., 2019). In order to satisfy the single-pool linear storage model, we considered only the convex part of the vegetation decay and referred to it as dry-down. In summary, the e-folding time of FVC is an emergent ecohydrological signature of the complex interactions between vegetation, climate, soil, and possibly groundwater.

To derive the ecohydrological metrics for the African continent from high-resolution remote sensing data (Sec. 2), we developed of a robust methodology (Sec. 3) to deal with noise, gaps, widely varying dynamics, and data size. The quality diagnostics along with the derived metrics (Sec. 4), and open code for derivations, enables future advances in understanding and modelling ecohydrological processes and variability. Initial analysis and corroboration with independent data illustrates the potential of applications of the ecohydrological metrics (Sec. 5).

2 Data

2.1 Fraction of Vegetation Cover

The FVC, derived from a spectral mixture analysis of the satellite retrievals, is a vegetation index summarising the coverage ratio of vegetation per unit total land area within a grid cell (Trigo et al., 2011). With a range of 0–1, FVC is often used to derive fundamental vegetation indices such as the Leaf Area Index. The FVC product used in this study was obtained from the Satellite Application Facility for Land Surface Analysis (LSA-SAF) of the European Organisation for the Exploitation of Meteorological Satellites (EUMETSAT). The product is based on the retrievals of the Spinning Enhanced Visible and Infrared Imager (SEVIRI) sensor on board the Meteosat Second Generation (MSG) satellite (Trigo et al., 2011). As a geostationary satellite, the MSG has a circular spatial coverage of Earth centred at 0° longitude, and it covers Europe and Africa entirely (see an example of the original FVC data for a day in Fig. A1). The SEVIRI is a multispectral optical sensor with 12 spectral bands, and a temporal resolution of 15 minutes. Under the sub-satellite point (nadir), it has 3.1 km spatial resolution in the normal bands, and a high-resolution band with 1 km spatial resolution. The spatial resolution of the retrieval decreases with distance from the nadir, as for all geostationary satellites. The FVC data product is available at daily temporal resolution spanning the time period from early 2004 to present. The FVC product, as well as its complete details, are available at https://landsaf.ipma.pt/en/products/vegetation/fvc/ .

For this study, we selected the spatial domain as the African continent. We resampled the original data to a spatial resolution of 0.0417° (∼ 5 km) with the nearest neighbour method (using gdalwarp function in GDAL (GDAL/OGR contributors, 2020)). In terms of temporal domain, we used nearly 16 years of data, from the beginning of the records in 2004, to the end of 2019.

2.2 Ancillary data

Climate:

To characterise major climate conditions, we used the Köppen–Geiger climate classification data (Rubel & Kottek, 2010) which is available at 0.0833° spatial resolution. For the sake of interpretability, we simplified the original climate classes into 6 major climate groups: arid desert (BW), arid steppe (BS), tropical humid (Af *&* Am), tropical with dry season (As *&* Aw), temperate humid (Cf), and temperate with dry season (Cs *&* Cw). A small number of grid cells with continental (D) or polar (E) climates around Mount Kilimanjaro were discarded. A map of the simplified climate classes can be found in Fig. D1.

Accessible water storage capacity and rooting depth:

We compared the integral metric (I_{ds}) against other proxies of plant accessible water. For that, we selected the rooting depth and plant available water storage capacity data from previous studies. For rooting depth, we used two data: Yang et al. (2016), at 0.5° spatial resolution, derived from a carbon cost–benefit model, and potential rooting depth data from Fan et al. (2017), at 0.0083° spatial resolution, derived with a plant adaption perspective via inverse modelling of root water uptake. For water storage capacity, we again used two datasets based on hydrological or land surface models: data from Tian et al. (2019) at 0.25° spatial resolution, and that from Wang-Erlandsson et al. (2016) at 0.5° spatial resolution. For a consistent comparison across data at different resolutions, we aggregated all data to a common spatial resolution of 0.5° by simple averaging. Note that the spatial aggregation may result in the loss of the spatial variability prevalent locally and potentially captured at a high resolution.

Topography:

To relate the variation of the metrics with local-scale heterogeneity and convergence of moisture caused by topography, we used the Height Above Nearest Drainage (HAND) data from Yamazaki et al. (2019). The HAND is a normalised metric derived from topography that is closely related with drainage topology and potential local-scale convergence of soil moisture and groundwater (Nobre et al., 2011). The HAND data used here is based on the MERIT digital elevation model at a spatial resolution of 3-arc second (∼ 90 m). We used the original high-resolution data after aggregating (simple average) to the resolution of our ecohydrological metrics (0.0417°).

Canopy height:

Since canopy height is an important indicator of ecosystem functions and is associated mostly with water limitation (Tao et al., 2016), we analysed the covariation of canopy height with the decay rate of vegetation cover during dry-down. We used the lidarderived canopy height data from the retrievals of the ICEsat satellite at a spatial resolution of 1 km (Simard et al., 2011). We used the data after aggregating (simple average) to 0.0417°.

3 Methodology

The derivation of the ecohydrological metrics (see Table 1) is based exclusively on the daily FVC time series. The method can be divided into four main steps: (i) masking and retrieval of minimum and maximum FVC (FVC_{min} and FVC_{max}), (ii) detection of start and end of the dry seasons (t_{ds}), (iii) estimation of the dry season FVC integral and duration (I_{ds} and D), and (iv) estimation of the FVC decay rate during dry-down (λ). Each methodological step is described in detail in the following subsections.

Table 1: A summary of ecohydrological metrics derived from FVC time series in this study.

Metric	**Quality Diagnostic**
Minimum asymptotic value of vegetation cover (FVC_{min})	-
Maximum asymptotic value of vegetation cover (FVC_{max})	
Duration of dry season (D)	Variation
Starting day of year of dry season (t_{ds})	Variation
Integral of time series of vegetation cover in dry season (I_{ds})	Variation
e-folding time of vegetation cover during dry-down (λ)	Variation, number of converged estimations

3.1 Masking and retrieval of minimum and maximum FVC

To remove the effect of outliers within a time series, we selected the 2nd and 98th percentiles of the entire records of the FVC data as the minimum (FVC_{min}) and the maximum asymptotic values (FVC_{max}). To maintain a reliable signal-to-noise ratio, we filtered out any grid cell with (i) $FVC_{max} < 0.1$ (ii) more than one-third of the time series were missing before further steps. Due to the simplicity of the derivation of FVC_{min} and FVC_{max} metrics, quality diagnostics were deemed unnecessary, and not derived in this set of metrics.

3.2 Detection of dry seasons

Detection of the dry season was based on a procedure using the first derivative of the smoothed FVC (V') (see Algorithm 1). We smoothed daily time series of the FVC with a 31-day moving average (V_{sm}). Then each day in the time series was marked as decay, recovery or stable. To do so, we set two thresholds for dry and wet seasons as th_{dry} and th_{wet}, respectively. We used the 75th and 70th percentiles of the negative derivative (V') as thresholds th_{dry} and $-th_{wet}$ for each grid cell. The magnitude th_{dry} is, thus, bigger than th_{wet}. Only the magnitude of th_{wet} was taken as a positive threshold to detect the increase in FVC.

An observation was considered as decay if $V' < th_{dry}$, recovery if $V' > th_{wet}$, and stable if $th_{dry} \leq V' \leq th_{wet}$. The resulting time series of classes (decay, stable, or recovery) were then smoothed by retaining the majority of decay and stable against recovery within a 5-day moving window. Dry season was then identified as the period from the beginning of a decay to the end of a stable period. In order to ensure the robustness of the end of the stable period, especially in hyper-arid regions with poor signal-to-noise ratio, we extended the detected dry seasons until the next significant increase in V_{sm} ($>$ 5% of the corresponding seasonal amplitude of FVC). Note that the selection of the thresholds and the moving window sizes were based on extensive exploration and visual inspection of the FVC time series. The exploration was a necessary step to ensure the robustness against noise in the data, as well to address the diversity of FVC dynamics across African ecosystems. To highlight the complexity, some representative time series of FVC in selected grid cells across different climates are included in Appendix Appendix B.

After detection of all dry seasons in the time series, we only selected the longest one per calendar year. This is necessary for regions where vegetation may potentially have two growing (and drying) seasons within a year. The longest dry season within a year is likely to be the most indicative of the largest water limitation, and the underlying ecohydrological mechanisms. When the detected dry season spanned over two calendar years, it was assigned as the dry season of the starting year. In total, the dry season detection algorithm (Algorithm 1) yielded 16,423,339 dry seasons in 1,029,847 grid cells.

Algorithm 1 Detection of dry seasons from the entire time series

1: Smooth FVC time series with 31 days moving average; to yield V_{sm}
2: Calculate the first derivative of FVC time series from V_{sm} with daily step size; to yield $V^{'}$
3: Through the entire time series, set the threshold for decay as th_{dry}=percentile($V^{'}$, 75) where $V^{'} < 0$
4: Through the entire time series, set the threshold for growth as th_{wet}=-1 $\times$ percentile($V^{'}$, 70) where $V^{'} < 0$
5: Mark each observation for their corresponding period as:
  if $V' < th_{dry}$ **then** decay
  else if $V' > th_{wet}$ **then** recovery
  else stable
6: Smooth the classes with a 5-day moving window by majority voting
7: Label consecutive observations marked with decay and followed by stable ones as *dry season*
8: Extend every *dry season* label until $V_{sm} > min(V_{sm}) + 0.05 \times (max(V_{sm}) - min(V_{sm}))$ is satisfied in the corresponding season
9: For each grid cell, keep only the longest *dry season* per year

3.3 Derivation of duration related metrics

We calculated the integral of FVC during dry season (I_{ds}) as the total area under the FVC time series from the start to end of the dry season, with the area under FVC_{min} removed. This can be expressed as,

$$I_{ds} = \sum^{dryseason} FVC(t) - FVC_{min} \tag{1}$$

Removal of the baseline FVC value (FVC_{min}) enhances the signal of seasonal decay of vegetation with respect to baseline vegetation activity. Note that, upon necessity, the full integral (total area under the curve) can be calculated as the sum of I_{ds} and $D\times FVC_{min}$.

From the yearly dry season detection, 16 (the number of years) values of D, t_{ds} and I_{ds} we computed for each grid cell. We selected the median of the 16 values as the representative inference to be used for spatial analyses. The median was preferred over the mean to make the estimation robust against annual variations, for instance, by intermittent rain events in the dry season or issues related to FVC derivation. In addition, we also calculate and report the normalised robust Standard Error (SE) as an indicator of variability. The SE is calculated as,

$$SE = \frac{SD_n}{\sqrt{n}} \tag{2}$$

where SD_n is the robust standard error, calculated from the Median Absolute Deviation (MAD) across years (with the assumption of a normal distribution, Rousseeuw & Croux, 1993), and corrected for the low number of samples ($n = 16$) as:

$$SD_n = MAD \times 1.4826 \times \frac{n}{n-1} \tag{3}$$

The robust standard error reflects variability of the metrics among years as well as methodological uncertainty, and is therefore suitable for customised filtering in the context of spatial analysis.

3.4 Derivation of exponential decay rate

Temporal decay of the FVC can be characterised using an exponential function as,

$$FVC = (FVC_{dd} - FVC_{min}) \times e^{-t/\lambda} + FVC_{min} \tag{4}$$

where FVC_{dd} is the initial FVC value in the beginning of a dry-down, and λ is the e-folding time (in days). Note that λ is merely an inverse of the exponential decay rate. The formulation in Eq. 4 uses λ as it is easier to interpret. In simple terms, λ denotes the number of days needed to have a decrease in the seasonal amplitude of FVC ($FVC_{dd} - FVC_{min}$) to $1/e$ of its original value during a dry-down event.

Due to the S-shaped character of temporal vegetation dynamics, functions allowing different convexity, e.g., logistic functions, have been used to characterise the vegetation decay. As exponential decay functions are strictly convex, the concave part of the decay is not considered in this study. Note that curvature is concave mostly at the beginning of dry season, which is of smaller relevance to the metrics presented here. In addition, the selected exponential decay function takes into account an asymptotic value of the FVC, as FVC_{min} (see Sec. 3.1) is explicitly included in the formulation (Eq. 4).

At the beginning of a dry season, when water demand of the ecosystem is still largely supported by surface soil moisture, the FVC typically does not decay at an exponential rate. To identify the dry-down period, for which λ is estimated, we infer insights from the mathematical properties of the exponential decay function. As the curvature of the exponential decay function is strictly convex, the first derivative is negative, and the second derivative is positive. Therefore, we first discarded the time steps with concave observations (negative first and negative second derivative). Afterwards, we filtered out the convex observations before the inflection point of the FVC, that mostly associated with low signal-to-noise ratio at the beginning of the dry-down. After marking the observations as either convex or concave, we searched for local minimum of V' in the first third of the dry season, and identified the inflection point as the start of the dry-down. Note that, in the above process, second derivative of the FVC (V'') was also smoothed with a 31-day moving window.

This procedure effectively removes observations with concave shape in the dry season, especially at the beginning of an event. For each event, if more than half of the data points showed convexity, we estimated λ, together with FVC_{dd}, based on an asymptotic regression model that minimises least squares error with the Levenberg–Marquardt algorithm (Moré, 1978; Elzhov et al., 2016)). We used both the Nash–Sutcliffe modelling efficiency (NSE; Nash & Sutcliffe, 1970) and the standard error of the model (SE_m) to assess the estimates of the model fitting. From the multiple λ estimates, only those with successful convergence of the Levenberg–Marquardt algorithm with $NSE > 0.5$ and $SE_m(\lambda) < 0.5 \times \lambda$ were selected, the median of which was taken as the representative final λ for a grid cell.

Algorithm 2 Identification of dry-down periods and modelling of the exponential decay

1: Smooth $V^{'}$ with 31 days moving average; to yield $V^{'}_{sm}$
2: Calculate the second derivative of FVC time series from $V^{'}_{sm}$ with daily step size; to yield $V^{''}$
3: Smooth $V^{''}$ with 31 days moving average; to yield $V^{''}_{sm}$
4: Mark each observation with $V^{'}_{sm} < 0$ as:
  if $V^{''}_{sm} > 0$ **then** convex
  else concave
5: Ignore convex observations before the inflection point of FVC time series, if there is any
6: Ignore concave observations within the dry season and keep the rest as the dry-down period
7: Discard any event having more concave observations than convex
8: Use Eq. 4 on dry-down period of the dry season to estimate λ
9: Filter out the estimations with $NSE < 0.5$ OR $SE_m(\lambda) > 0.5 \times \lambda$

After defining the final λ, we estimated the variation as done in Sec. 3.3. Unlike in Sec. 3.3, the sample size per grid cell (n) may change, as λ estimation may not converge in cases with high noise. We, therefore, also report the number of successful convergences of the Algorithm 2 as an additional quality diagnostic that can be used for filtering λ (mapped in Fig. G1).

4 Ecohydrological metrics from vegetation time series dynamics

In this section, we present and discuss the ecohydrological metrics derived in this study (see Table 1). Here we present the metrics independently, but we summarise their cross-comparison in Fig. C1. For each metric we show the variation in continental scale by maps along with zoomed inset plots (see Sec. Appendix D for further information and visual impression by corresponding Google Earth cut-outs) to visualise regional variability. Box plots for major bioclimatic regions (see Sec. 2.2 for the definition) provide insights on the co-variation with large scale climate.

4.1 Minimum and maximum FVC

The spatial distributions of FVC_{min} and FVC_{max}, histograms of the distribution in the full domain, and six zoomed insets focusing on selected regions are shown in Fig. 2a and 2b (see Fig. E1 for the seasonal dynamics expressed as $FVC_{max} - FVC_{min}$). At the continental scale, both FVC_{min} and FVC_{max} follow the climate gradient with the highest and the lowest values in humid and arid regions, respectively. Nevertheless, compared to FVC_{max}, FVC_{min} has a stronger spatial gradient associated with climate seasonality within each major climate group (see Fig. 2c). Understandably, the climatic groups with a distinct dry season have a lower FVC_{min}. This highlights the effect of water limitation on vegetation dynamics in regions with distinct seasonality of water availability (see Fig. D1 for map of simplified climate classes as well as Google Earth views of the insets).

In addition to the climate-associated large scale gradients, the metrics also exhibit a substantial local-scale heterogeneity. In arid regions, FVC_{min} is higher in areas closer to the water sources, as can be seen near the Senegal and Gambia rivers (Box-A in Fig. 2a). Positive effect of seasonal flooding on FVC_{min} is also evident near large inland deltas (e.g., the Okavango Delta and the Sudd swamp, Box-D and Box-F in Fig. 2a, respectively). Such local-scale heterogeneity clearly exhibits the importance of secondary water sources in water-limited systems, especially on top of the large climate-driven spatial variations, and highlights the usefulness of vegetation-based asymptotic metrics for ecohydrological studies.

4.2 Dry season duration related metrics

The dry season duration, D, also follows the climatic gradient at the continental scale, with the shortest dry season in tropical humid, the longest in arid, and intermediate values in the temperate climates (Fig. 3a). Even for tropical and temperate climate, D consistently increases when the sub-climate includes a dry season (Fig. 3c). The decrease in D from arid steppe to arid desert climate suggests that the Algorithm 1 may still be sensitive to very low signal-to-noise ratios in some of the hyper-arid regions with low FVC and rare, episodic rainfall. Though, such occurrences can be well identified and filtered using the variation of D, as the values in some hyper-arid regions are relatively high (Fig. 3b).

At local scales, variations in D emerge as a combined effect of climate and other local ecohydrological factors, such as proximity to the nearest drainage or occurrences of shallow water table depth. This, once again, is particularly the case in semi-arid climates. For example, shorter dry seasons appear in seasonally flooded areas like Barotse Floodplain, the Okavango Delta, and the Sudd swamp, where shallow water tables of the floodplains support vegetation for longer periods (Box-D and Box-F in Fig. 3a). In these regions, lateral water transport and moisture convergence in the floodplains provide an important buffer for vegetation against the climate-driven dryness, which would not be detectable from precipitation data.

I_{ds} shows on average smaller values in humid tropical and arid desert compared to the other climates of intermediate dryness. However, variation of I_{ds} within climate groups is much larger when subject to intermediate dryness (Fig. 4a and 4c). The regional inset plots show the impact of shorter dry season duration on I_{ds} in seasonally flooding wetlands (Box-D and Box-F of Fig. 4a). However, I_{ds} does not only follow the patterns of D. For example, the variation of I_{ds} in the Lower Zambezi and its tributaries does not coincide with that of D (Box-E of Fig. 4a and Fig. 3a). The highest values of I_{ds} in the Lower Zambezi, bear strong similarity with the rooting depth product of (Wang-Erlandsson et al., 2016), and the previously reported seasonal hydrologic buffer (Kuppel et al., 2017) in these regions (see Sec. 5.1 for further corroborations).

4.3 Exponential decay rate

The λ, presented in Fig. 5a, has a mean value of 41 days with a positively-skewed distribution at the continental scale. We find the lowest λ values throughout the humid regions and partially in the arid regions, such as edges of the Sahara desert or the Horn of Africa. The highest λ values are found in the semi-arid and arid regions. Though variation of λ (Fig. 5b) suggests that the low values of λ in some hyper-arid regions are associated with higher uncertainty due to low signal-to-noise ratio.

Besides the coherent continental-scale spatial patterns, λ also has strong variations at the local scale. Stronger lateral moisture convergence positively affects the λ in the arid regions, as seen in the Senegal (Box-A, Fig. 5a) and the Niger (partially in Box-B, Fig. 5a) rivers in the arid climate. However, lateral moisture convergence does not always affect λ positively, as seen in the Upper Zambezi and the Okavango rivers and their tributaries. The λ is high around the Cuando river, the Okavango Delta and the Linyati swamp, but low in the Barotse Floodplain (Box-D in Fig. 5a). Such non-trivial patterns suggest the role of complex interactions between the vegetation traits and local moisture conditions (Fan et al., 2019), which also effect λ (see Sec. 5.2 for further corroborations and discussions).

5 Corroborating products and potential applications

5.1 Relationship between I_{ds} and plant available soil water holding capacity

Conceptually, plant water storage capacity is related to the vertical distribution of roots, and the water holding capacity of the soil that is determined largely by texture and organic carbon content. The root profile of water-limited ecosystems appears to adapt to the prevailing hydrologic and soil conditions while being constrained by other ecosystem properties and traits (Guswa, 2008; van Wijk, 2011; Fan et al., 2017; Schenk, 2008; Schenk & Jackson, 2002; Laio et al., 2006). Plant water storage capacity controls the propensity and sensitivity of ecosystems to drought stress in dry periods. Various modelling approaches to infer rooting depth or plant water storage capacity have been proposed (explained in detail in Wang-Erlandsson et al., 2016), as it cannot be observed directly but still contains a critical information for global-scale models (Kleidon & Heimann, 1998).

The integral of the FVC during dry season should be positively correlated with plant accessible water storage of the soil, as larger water storage would facilitate vegetation activity for longer period during water-limited conditions. The continental scale pattern of I_{ds} (Fig. 4a) with the largest values in strongly seasonal semi-arid Savannah systems of both hemispheres is qualitatively consistent with the previous observation-based analysis (e.g. Schenk & Jackson, 2002) as well as the optimality-based models (e.g. Kleidon & Heimann, 1998). I_{ds} declines in hyper-arid regions like the Sahel, Horn of Africa, Southern Africa, as well as the Congo rainforest. A similar pattern would be expected for optimal rooting depth, which increases in regions with small differences between rainfall and potential evaporation in annual scales but large differences in seasonal scales (Laio et al., 2006; van Wijk, 2011). The inset plots in Fig. 4a clearly reveal the landscape scale patterns of I_{ds}, presumably, due to topography-driven large variations of moisture. This may reflect enhanced and continued moisture supply due to topographic moisture convergence or shallow water tables along with possible adaptations of rooting depth to these local hydrological conditions (Fan et al., 2017).

We compared I_{ds} with 4 products of plant storage capacity (Wang-Erlandsson et al., 2016; Tian et al., 2019) or rooting depth (Yang et al., 2016; Fan et al., 2017) at 0.5° across Africa. As shown in Fig. H1, there is qualitative agreement of high values of I_{ds} and the storage capacity from Tian et al. (2019) and Wang-Erlandsson et al. (2016) in the Miombo woodlands and, to a lesser extent, also in the northern savannahs. All three also agree on low values in hyper-arid regions like the Sahel, Horn of Africa and in Southern Africa. A pairwise comparison of Spearmans correlation coefficient among the five estimates (Fig. 6) reveals that the strongest agreement is between I_{ds} and storage capacity from Wang-Erlandsson et al. (2016). The overall low-to-moderate correlation values among the previous observation-based products demonstrates the scale of the challenge in estimating plant water storage capacity or rooting depth (Fig. 6).

All four independent products utilised meteorological input data for water balance estimation, and also use remotely-sensed vegetation products in some way. While the products of Wang-Erlandsson et al. (2016) and Tian et al. (2019) are constrained by hydrological earth observations, the rooting depth products of Fan et al. (2017) and Yang et al. (2016) originate largely from different assumptions of optimality and plant adaptation. Our comparison suggests that estimating plant storage capacity based on Earth observation data may be more suitable than the presently-used optimality principles. Using I_{ds} as an indicator of plant water storage capacity has the advantage that it is derived from dense time series of a geostationary satellite alone, requiring no additional meteorological inputs or modelling assumptions that introduce their inherent uncertainties. In a sense, the remote sensing based I_{ds} is directly associated with the actual vegetation growth, and is completely independent of the assumptions and uncertainties of theoretical models or meteorological dataset. Furthermore, I_{ds} features much higher spatial resolution than most other storage capacity data, which provides insights in the role of topography-driven subsurface moisture variations.

There are many factors other than plant water storage capacity that could influence I_{ds}. Therefore we compared the variation of I_{ds} with the HAND data in different climate groups to find associations of I_{ds} with topographically induced moisture variations (Fig. 7). In dry regions, I_{ds} tends to decline with increasing HAND, apparently above a varying HAND threshold. This implies that shallow water tables may support vegetation with additional moisture availability under dry conditions, as also shown in Koirala et al. (2017). Therefore, I_{ds} is a suitable proxy for analysing the complex patterns and processes surrounding groundwater–soil moisture–vegetation interactions.

5.2 λ and canopy height

The rate of FVC decay during dry-down events, λ, can corroborate to the rate of decrease of plant available water, ecosystem scale water use efficiency, and the propensity to senescence. Ecosystems differ widely in their water use strategies, from being water conservative – typically associated with strong down-regulation of stomatal conductance with water deficiency – to aggressive exploitation of water resources (Laio et al., 2001). Herbaceous plants are typically aggressive water users and cease with the depletion of surface soil moisture. Woody plants risk cavitation and death under severe water stress, and such, trees in places with frequent dry periods benefit from a water saving strategy or senescence for prolonged periods. Konings and Gentine (2017) inferred ecosystem water-use strategies globally based on diurnal variations of vegetation optical depth assuming that those reflect stomatal regulation to maintain leaf-water potential. They found an increase in isohydricity, the degree of stomatal regulation and subsequent water savings, with increase in vegetation height, consistent with the need of tall trees to prevent hydraulic failure during drought.

If the rate of FVC decay was also related to the ecosystems' water use strategy in a similar manner, we would expect slower FVC decay (higher λ) with increasing canopy height. For arid regions, we indeed find a tendency of increasing λ with canopy height (Fig. 8), suggesting that λ incorporates ecosystem water use strategy traits as well as direct/indirect effects of soil moisture therein. However, as the climate gets wetter, or over the entire African continent, λ tends to decrease with canopy height. A possible explanation would be that water consumption, i.e. transpiration, increases with canopy height resulting in a faster depletion of moisture storage (Koirala et al., 2017), or increasing ecosystem water use efficiency with aridity. Even though interpretation of the spatial variability of λ remains speculative at this point, the initial analysis and considerations given here show the potential of gaining ecohydrological insights, especially for model-data-fusion exercises.

6 Conclusions and outlook

Using retrievals of the SEVIRI sensor of the geostationary satellite MSG, we derived ecohydrological metrics for continental Africa entirely from the temporal dynamics of the daily Fraction of Vegetation Cover (FVC) time series from 2004 to 2019 at 0.0417° spatial resolution. Our metrics captures both, continental scale gradients and covariations with climate as well as structured regional variations, e.g. due to topographic factors. This provides an unprecedented opportunity to improve our understanding of ecohydrological processes across spatial scales over Africa.

The minimum asymptotic value of vegetation cover (FVC_{min}) gives indications on where secondary water resources support vegetation in the dry season. Duration and starting day of the dry season (D and t_{ds}, respectively) show the effective extent and start of the water-limited period, a critical source of information for any ecohydrological analysis or model study. Because they incorporate the effects of non-climatic factors as well, they are complementary to e.g. precipitation-based dry season delineations and have further the advantage that they can be estimated at higher spatial resolutions. The integral of FVC time series in dry season (I_{ds}) indicates buffering capacity of vegetation on moisture limitation and shows broad consistency with inferred variations of the plant storage capacity or rooting depth. Since this is an important, but at the same time a very uncertain, aspect in ecohydrology, our high-resolution estimate of I_{ds} may help understand and model ecohydrological processes more accurately. The spatial patterns of I_{ds} may be used to analyse plant water storage capacity in ecohydrological models and replace simplistic approaches where this varies only with vegetation type and soil. Finally, the e-folding time of vegetation cover during dry-down (λ) reveals the decay rate of vegetation during dry season, which emerges from the complex ecohydrological interactions. Using the structured but highly variable spatial patterns of λ, we believe much can be learned about underlying mechanisms by thorough analysis and modelling studies. The suggested algorithms for deriving the metrics and the provision of the code facilitates consistent parallel assessments and helps overcome the technical difficulties of dealing with large volumes of data and the particularities of vegetation cover retrievals from the geostationary satellites. There remain multiple opportunities for further synergistic exploitation with retrievals of surface temperature from geostationary satellites which could provide complementary indicators on variations of moisture states inferred from an energy balance perspective.

7 Data and code availability

All ecohydrological metrics and their quality diagnostics derived and presented in this study are available in standardised netCDF data format in `https://doi.org/10.17871/bgi_ehydro_afr_2020` (use `ftp://ftp.bgc-jena.mpg.de/pub/outgoing/ckucuk/ecoHydro_Afr` to download the data anonymously) (Küçük et al., 2020).

The R scripts developed for the implementation of the methodology are available for research uses. They can be accessed through `https://github.com/caglarkucuk/EcohydroMetrics_Africa.git` (also at `ftp://ftp.bgc-jena.mpg.de/pub/outgoing/ckucuk/EcohydroMetrics_Africa_Repository.zip` to ensure anonymity) and cited as Küçük et al. (2020).

The ancillary data from Tian et al. (2019) was obtained by contacting to the corresponding author. All other datasets were obtained from the public domain using the information in the cited literature (see Sec. 2).

Acknowledgments

Çağlar Küçük acknowledges funding from the International Max Planck Research School for Global Biogeochemical Cycles. Diego G. Miralles acknowledges funding from the European Research Council (ERC) under grant agreement 715254 (DRY2DRY).

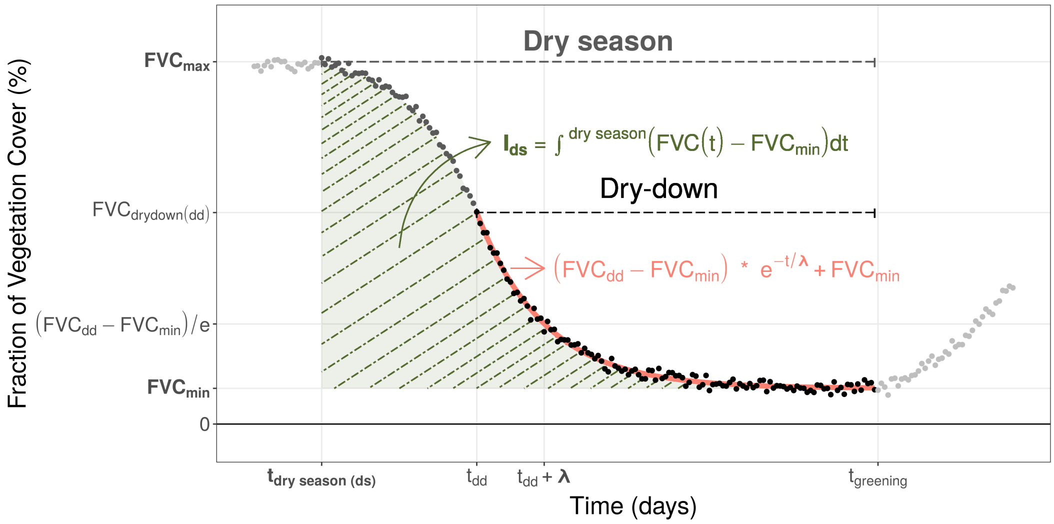

Figure 1: Conceptual plot of the ecohydrological metrics derived from time series using synthetic data. Points represent observations for wet season, early dry season and dry season with dry-down in light grey, grey and black, respectively. Dry and wet seasons are defined by presence of decay, i.e., first derivative of the time series, while dry-down period is defined by the convexity of the decay, i.e., using both first and second derivatives (see Sec. 3.4 for details). The shaded area shows the integral of FVC during dry season. The curve shows the fitted line on the FVC time series during dry-down using the asymptotic exponential decay function. All metrics presented in this study are shown in bold characters.

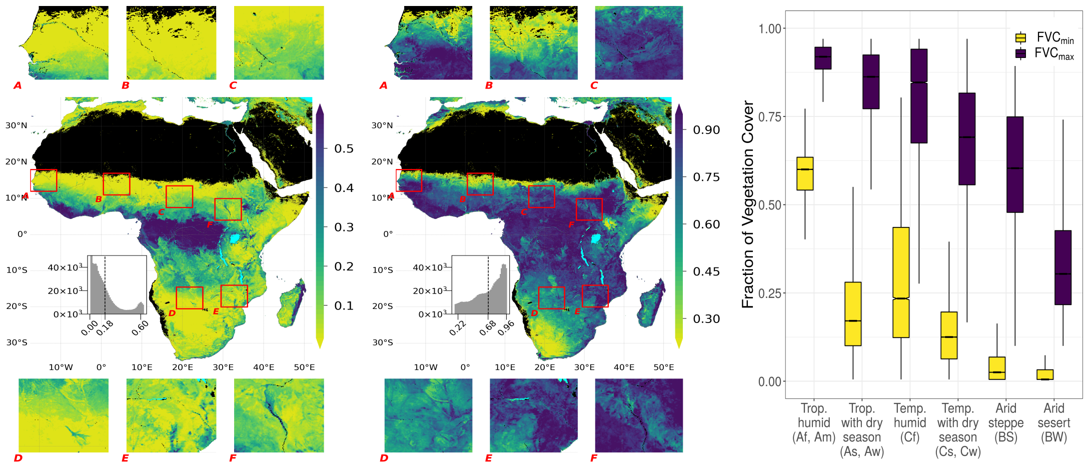

(a) (b) (c)

Figure 2: (a) Minimum asymptotic values of FVC, FVC_{min}, (b) maximum asymptotic values of FVC, FVC_{max}, (c) box plot showing the distribution of FVC_{min} and FVC_{max} in different climate groups. A histogram of the metrics mapped can be seen inside the major plot, with a dashed line indicating the mean values of the domain in all maps. See Sec. Appendix D for further explanation of the insets in the map. In all of the following box plots, median values per class are shown in the intermediate line of the boxes, with their 95 % confidence intervals notched. Upper and lower edges of the boxes show the interquartile range (75th and 25th percentiles, respectively) while the error bars show 1.5 times the interquartile range.

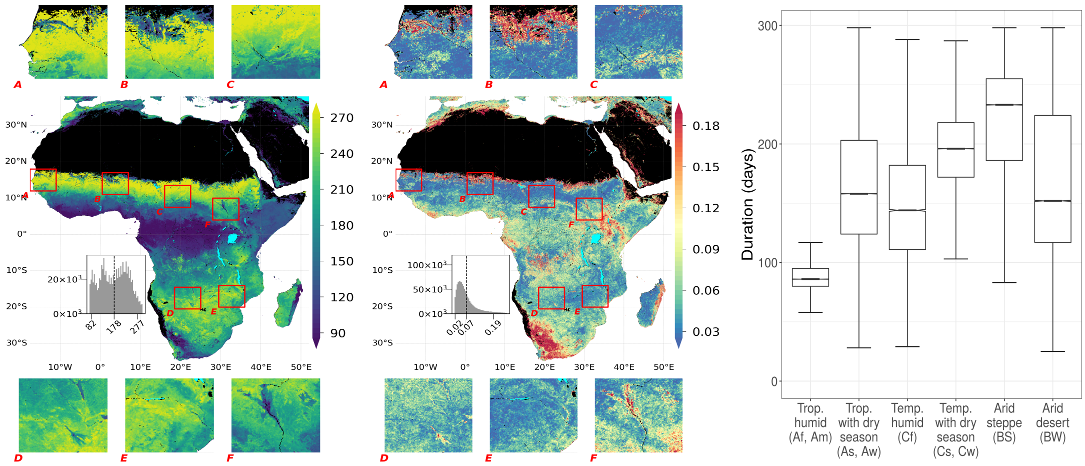

(a) (b) (c)

Figure 3: (a) Duration of the dry season (in days), D, (b) variation of D, (c) distribution of D within climate groups (see Fig. 2c for plotting details).

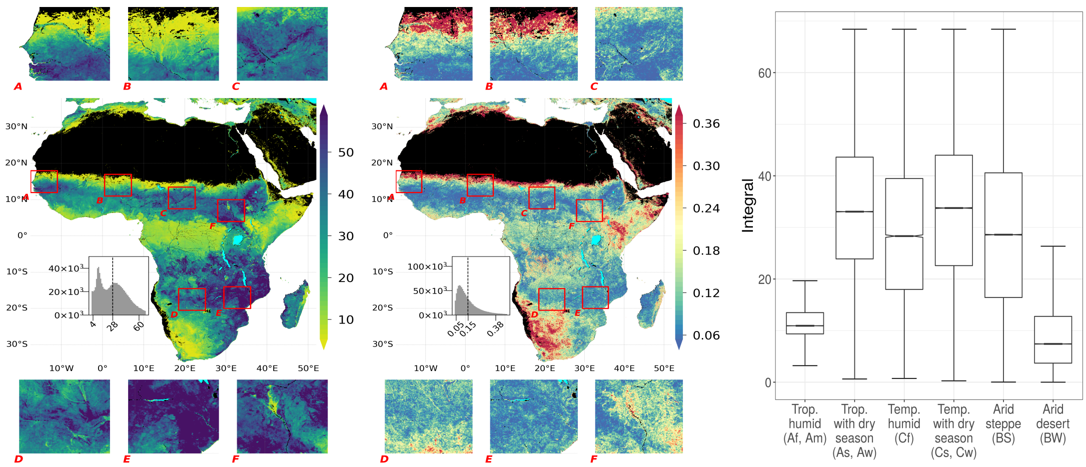

(a) (b) (c)

Figure 4: (a) Integral of FVC time series in the dry season, I_{ds}, (b) variation of I_{ds}, (c) distribution of I_{ds} within climate groups (see Fig. 2c for plotting details).

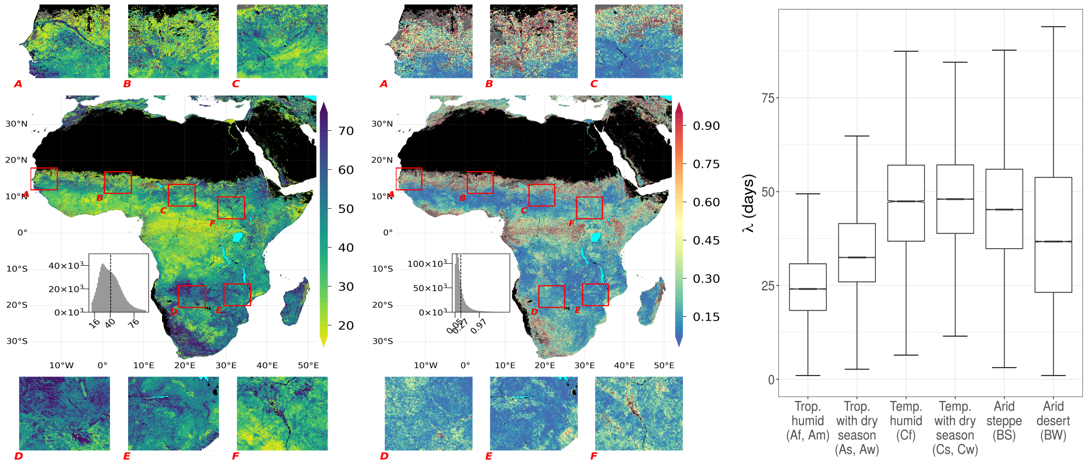

(a) (b) (c)

Figure 5: (a) e-folding time of FVC time series during dry-down (in days), λ, (b) variation of λ, (c) distribution of λ within climate groups (see Fig. 2c for plotting details).

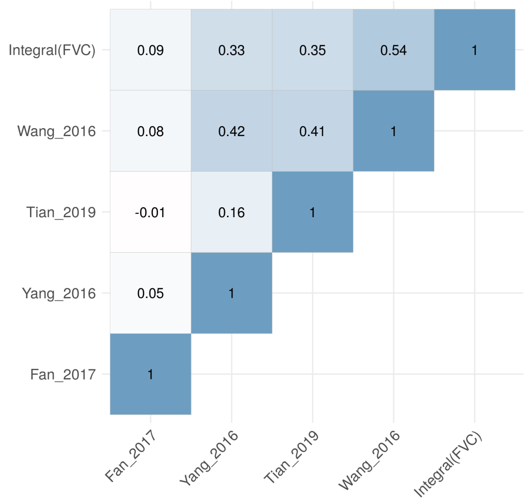

Figure 6: Spearman's correlation coefficients between different plant available water storage products.

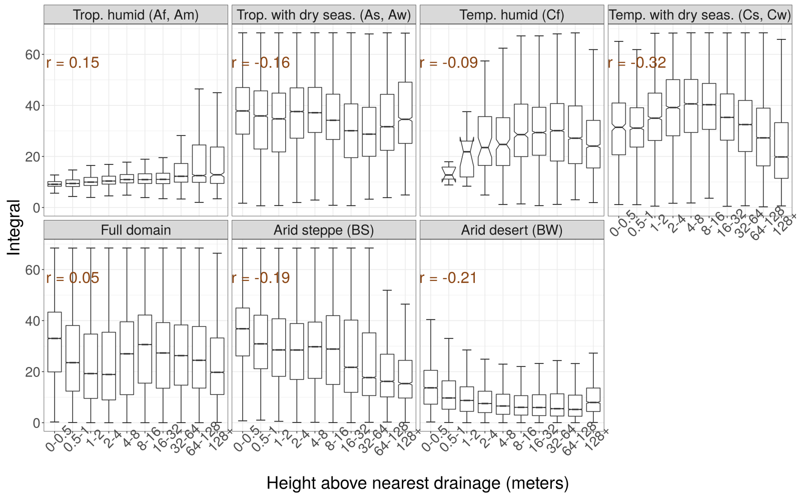

Figure 7: Covariation of I_{ds} and HAND for different climate groups, and for the full study domain. Spearman's correlation coefficients between I_{ds} and HAND are annotated in the panels.

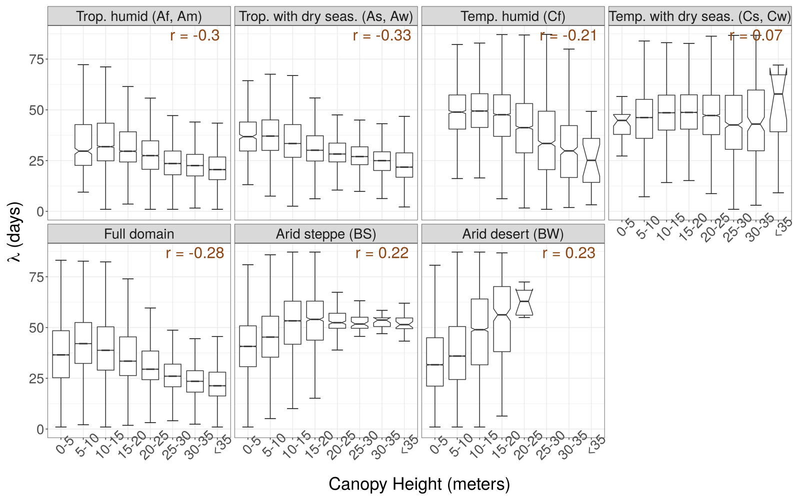

Figure 8: Covariation of λ and canopy height for different climate groups, and for the full study domain. Spearman's correlation coefficients between λ and canopy height are annotated in the panels.

Appendix A An example map of the original FVC data for a single day

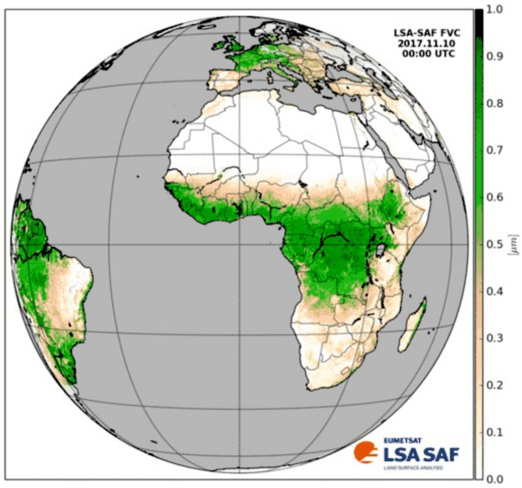

Figure A1: The original FVC data product for a single day, taken from https://landsaf.ipma.pt/en/products/vegetation/fvc/

Appendix B Time series of FVC in example grid cells

In this subsection; we present 5 years time series of two selected grid cells from each simplified climate class to demonstrate the results of the algorithms in grid cell scale.

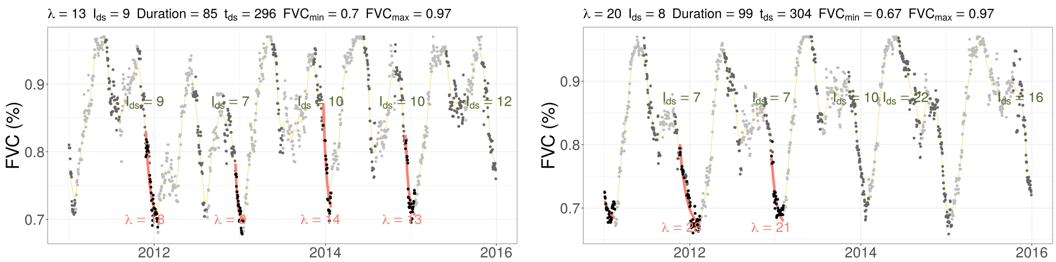

Figure B1: Time series of two grid cells from tropical humid climate (Af, Am) with coordinates (23.645832, 2.562501) and (29.145832, 2.562501), respectively. Seasonal values of λ and I_{ds} are shown inside the plot while final values of the metrics are given in the plot titles.

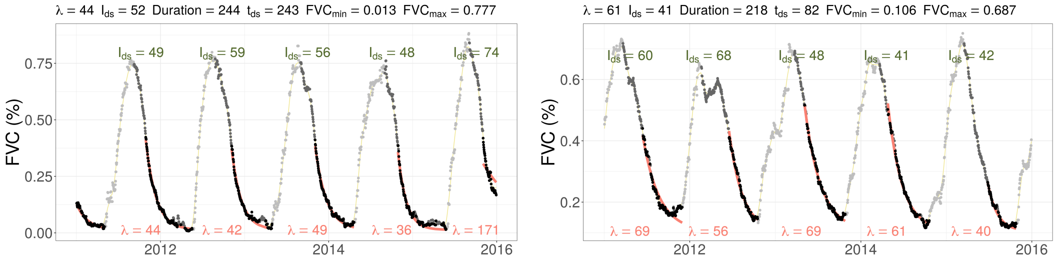

Figure B2: Time series of two grid cells from tropical climate with dry season (As, Aw) with coordinates (9.562499, 10.145834)) and (45.812498, -24.479165), respectively. Seasonal values of λ and I_{ds} are shown inside the plot while final values of the metrics are given in the plot titles.

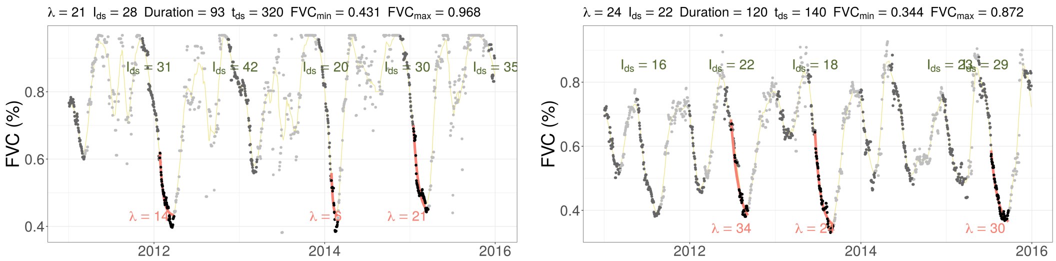

Figure B3: Time series of two grid cells from temperate humid climate (Cf) with coordinates (36.520832, 7.020834) and (30.104165, -1.104165), respectively. Seasonal values of λ and I_{ds} are shown inside the plot while final values of the metrics are given in the plot titles.

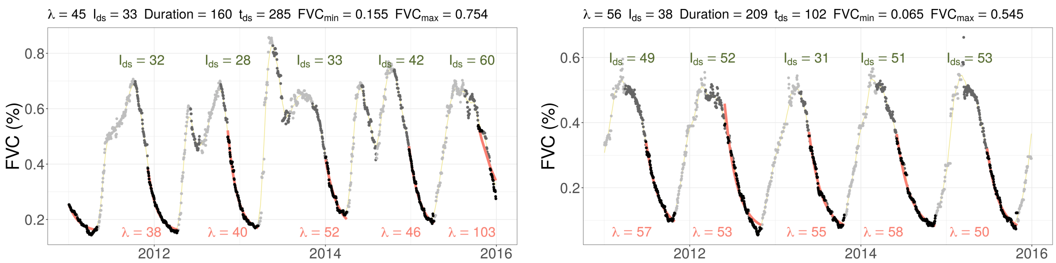

Figure B4: Time series of two grid cells from temperate climate with dry season (Cs, Cw) with coordinates (41.729165, 8.937501)) and (47.020831, -20.312498), respectively. Seasonal values of λ and I_{ds} are shown inside the plot while final values of the metrics are given in the plot titles.

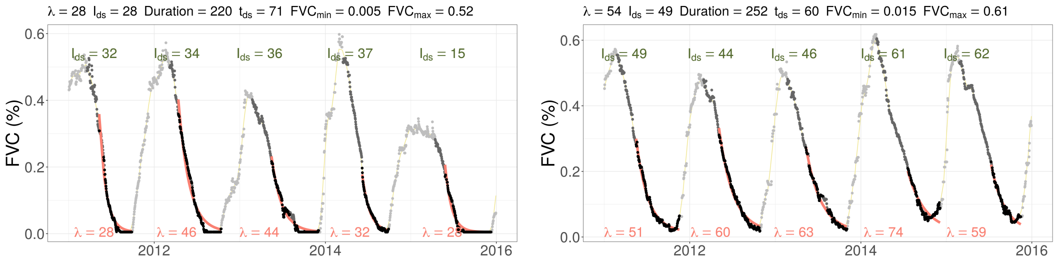

Figure B5: Time series of two grid cells from arid climate with steppe land cover (BS) with coordinates (18.354165, -20.229165) and (30.104165, -18.854165), respectively. Seasonal values of λ and I_{ds} are shown inside the plot while final values of the metrics are given in the plot titles.

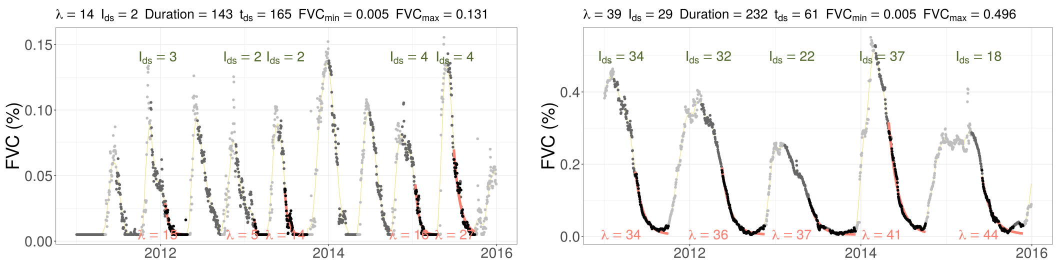

Figure B6: Time series of two grid cells from arid climate with desert land cover (BW) with coordinates (49.395831, 7.479168) and (19.645832, -21.520832), respectively. Seasonal values of λ and I_{ds} are shown inside the plot while final values of the metrics are given in the plot titles.

537 Appendix C Density plots of the ecohydrological metrics

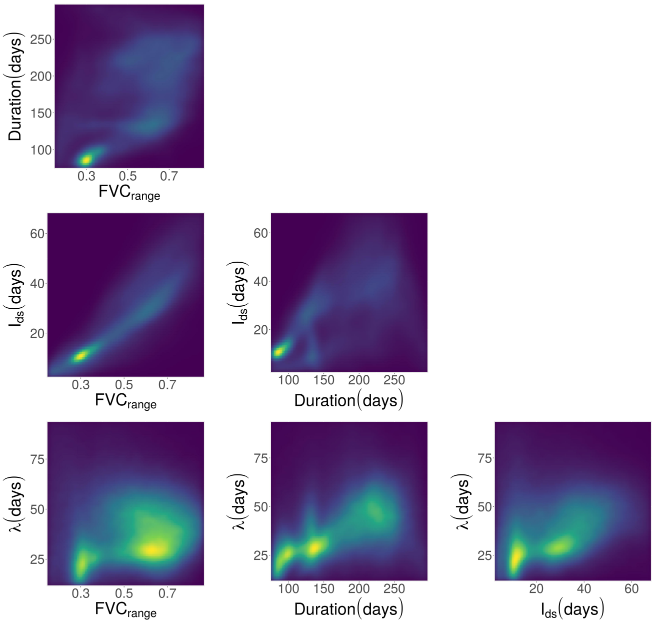

Figure C1: Density plots of the ecohydrological metrics presented in this study. $FVC_{range} = FVC_{max} - FVC_{min}$ is used to summarise the minimum and maximum FVC values.

538 Appendix D Map of simplified climate classes and Google Earth view
539 of insets

540 Fig. D1 shows the continental map of the simplified climate classes and the Google
541 Earth views of the insets. Box-A: the Gambia and most of the Senegal rivers; Box-B:
542 a small area of the Niger river mostly showing the transition from the Sahara desert to
543 Sahel; Box-C: more on the transition from Sahel to tropical regions; Box-D: located in
544 one of the most complex regions of Africa in terms of topography and lateral flow of wa-
545 ter with lower sections of the Okavango and the Cuando rivers and upper section of the
546 Zambezi river, together with multiple seasonally flooding areas like the Okavango delta,
547 the Linyati swamp and the Barotse Floodplain. These seasonal wetlands are vital for the
548 ecosystem and also provides great support against water limitation and heat for not only
549 plants but also animals; Box-E: Lower Zambezi Basin together with the drainage of Lake
550 Malawi to Zambezi. It also covers the Inyanga mountains located between Mozambique
551 and Zimbabwe where a climatic shift happens due to the mountain range. Last but not
552 least, Box-F, which is divided by the White Nile from South to North, covers the Sudd
553 swamp with a climatic gradient from tropical to arid systems.

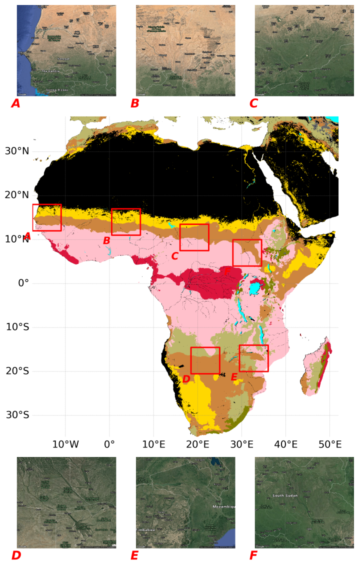

Figure D1: Map of simplified climate classes (from Köppen–Geiger climate classification) in the centre and satellite view of the insets. Map and image data of the insets: Google Earth ©2020 TerraMetrics.

Appendix E Map of FVC_{range} to show insights of FVC_{min} and FVC_{max}

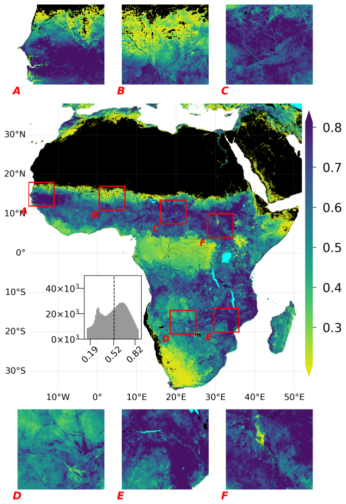

Figure E1: $FVC_{range} = FVC_{max} - FVC_{min}$

Appendix F Map of starting day of year of dry season

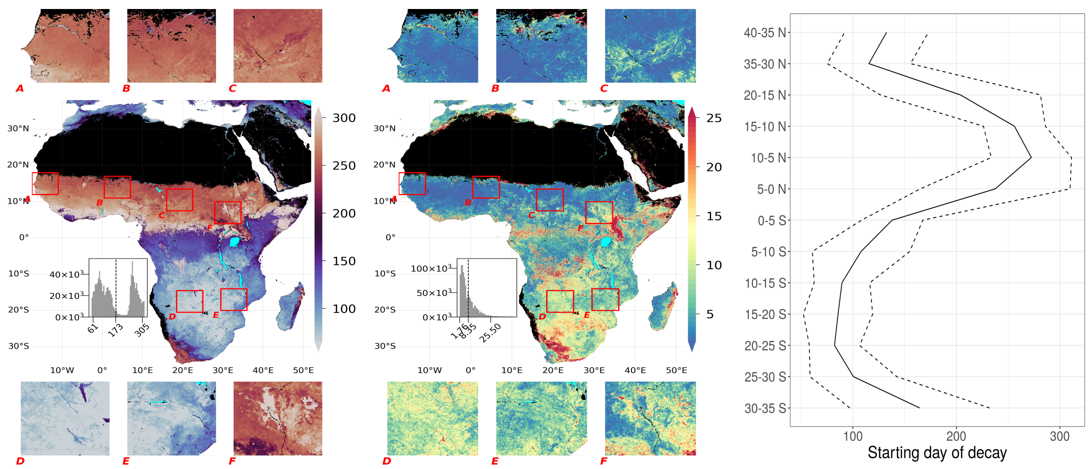

(a) (b) (c)

Figure F1: (a) Starting day of the dry season, t_{ds}, (b) SE of t_{ds} across years as a quality diagnostic, (c) latitudinal distribution of t_{ds}, where mean values per bin shown with continuous while standard deviations are shown with dashed lines.

Appendix G Map of number of convergences of Algorithm 2

Appendix H Maps of accessible water storage capacity datasets

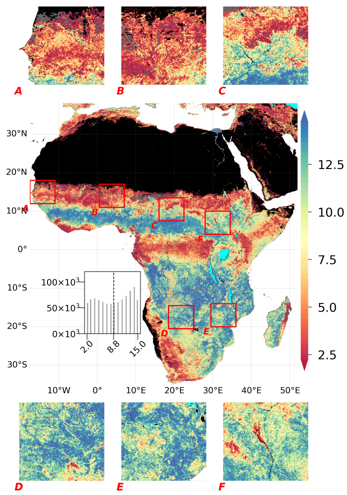

Figure G1: Number of dry seasons in which the Algorithm 2 successfully converged.

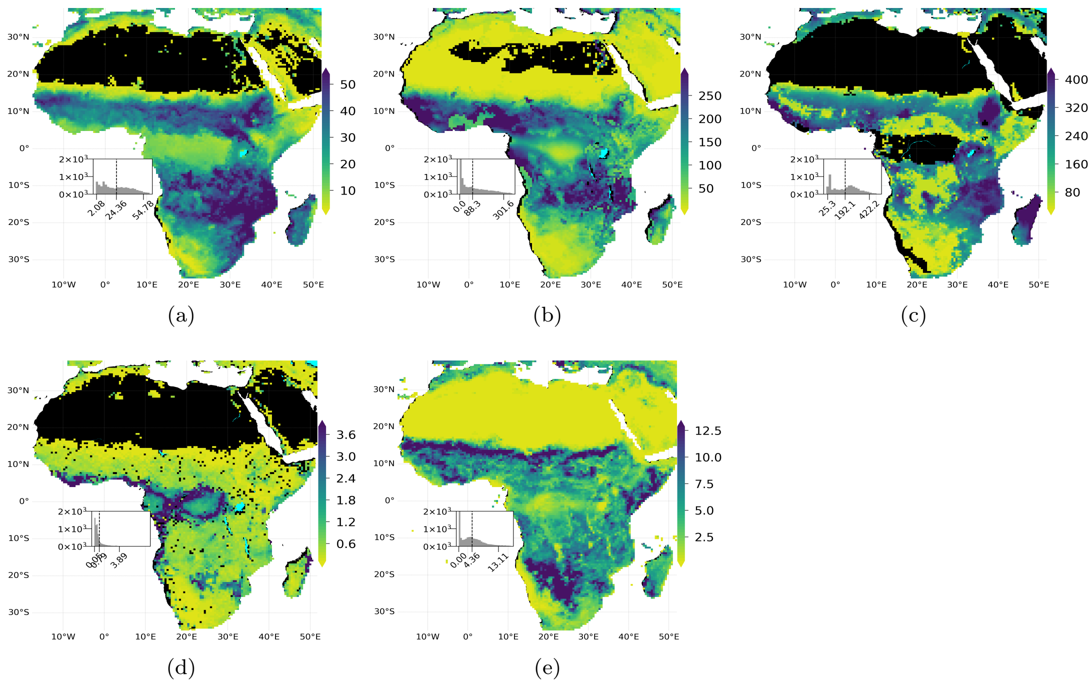

Figure H1: Maps of accessible water storage capacity and rooting depth datasets used in this study. (a) Integrated FVC during dry season, I_{ds}, (b) root zone storage capacity with CRU precipitation data with 2 years of drought return period from Wang-Erlandsson et al., 2016, (c) accessible water storage capacity from Tian et al., 2019 (d) effective rooting depth from Yang et al., 2016, (e) rooting depth from Fan et al., 2017. All products are aggregated to 0.5° and cropped for the study domain.

References

Boese, S., Jung, M., Carvalhais, N., Teuling, A. J., & Reichstein, M. (2019). Carbon-water flux coupling under progressive drought. *Biogeosciences*, *16*(13), 2557–2572. doi: 10.5194/bg-16-2557-2019

Caylor, K. K., Scanlon, T. M., & Rodriguez-Iturbe, I. (2009). Ecohydrological optimization of pattern and processes in water-limited ecosystems: A trade-off-based hypothesis. *Water Resources Research*, *45*(8), 1–15. doi: 10.1029/2008WR007230

Clark, M. P., Fan, Y., Lawrence, D. M., Adam, J. C., Bolster, D., Gochis, D. J., ... Zeng, X. (2015). Improving the representation of hydrologic processes in Earth System Models. *Water Resources Research*, *51*(8), 5929–5956. doi: 10.1002/2015WR017096

Elzhov, T. V., Mullen, K. M., Spiess, A.-N., & Bolker, B. (2016). minpack.lm: R Interface to the Levenberg-Marquardt Nonlinear Least-Squares Algorithm Found in MINPACK, Plus Support for Bounds [Computer software manual]. Retrieved from `https://cran.r-project.org/package=minpack.lm`

Fan, Y., Clark, M., Lawrence, D. M., Swenson, S., Band, L. E., Brantley, S. L., ... Yamazaki, D. (2019). Hillslope Hydrology in Global Change Research and Earth System Modeling. *Water Resources Research*, 1737–1772. doi: 10.1029/2018WR023903

Fan, Y., Miguez-Macho, G., Jobbágy, E. G., Jackson, R. B., & Otero-Casal, C. (2017). Hydrologic regulation of plant rooting depth. *Proceedings of the National Academy of Sciences*, *114*(40), 10572–10577. doi: 10.1073/pnas.1712381114

Fisher, R. A., & Koven, C. D. (2020). Perspectives on the future of Land Surface Models and the challenges of representing complex terrestrial systems. *Journal of Advances in Modeling Earth Systems*. doi: 10.1029/2018ms001453

GDAL/OGR contributors. (2020). GDAL/OGR geospatial data abstraction software library [Computer software manual]. Retrieved from `https://gdal.org`

Gentine, P., D'Odorico, P., Lintner, B. R., Sivandran, G., & Salvucci, G. (2012). Interdependence of climate, soil, and vegetation as constrained by the Budyko curve. *Geophysical Research Letters*, *39*(19), 2–7. doi: 10.1029/2012GL053492

Good, S. P., & Caylor, K. K. (2011). Climatological determinants of woody cover in Africa. *Proceedings of the National Academy of Sciences of the United States of America*, *108*(12), 4902–4907. doi: 10.1073/pnas.1013100108

Guan, K., Pan, M., Li, H., Wolf, A., Wu, J., Medvigy, D., ... Lyapustin, A. I. (2015). Photosynthetic seasonality of global tropical forests constrained by hydroclimate. *Nature Geoscience*, *8*(4), 284–289. doi: 10.1038/ngeo2382

Guswa, A. J. (2008). The influence of climate on root depth: A carbon cost-benefit analysis. *Water Resources Research*, *44*(2), 1–11. doi: 10.1029/2007WR006384

Kleidon, A., & Heimann, M. (1998). A method of determining rooting depth from a terrestrial biosphere model and its impacts on the global water and carbon cycle. *Global Change Biology*, *4*(3), 275–286. doi: 10.1046/j.1365-2486.1998.00152.x

Koirala, S., Jung, M., Reichstein, M., de Graaf, I. E., Camps-Valls, G., Ichii, K., ... Carvalhais, N. (2017). Global distribution of groundwater-vegetation spatial covariation. *Geophysical Research Letters*, *44*(9), 4134–4142. doi: 10.1002/2017GL072885

Konings, A. G., & Gentine, P. (2017). Global variations in ecosystem-scale isohydricity. *Global Change Biology*, *23*(2), 891–905. doi: 10.1111/gcb.13389

Küçük, Ç., Koirala, S., Carvalhais, N., Miralles, D. G., Reichstein, M., & Jung, M. (2020). Characterising the response of vegetation cover to water limitation in

Africa using geostationary satellites. *MPI-BGC Data Exchange Portal*. doi: 10.17871/bgi_ehydro_afr_2020

Kuppel, S., Fan, Y., & Jobbágy, E. G. (2017). Seasonal hydrologic buffer on continents: Patterns, drivers and ecological benefits. *Advances in Water Resources*, *102*, 178–187. doi: 10.1016/j.advwatres.2017.01.004

Laio, F., D'Odorico, P., & Ridolfi, L. (2006). An analytical model to relate the vertical root distribution to climate and soil properties. *Geophysical Research Letters*, *33*(18), 1–5. doi: 10.1029/2006GL027331

Laio, F., Porporato, A., Fernandez-Illescas, C. P., & Rodriguez-Iturbe, I. (2001). Plants in water-controlled ecosystems: Active role in hydrologic processes and response to water stress IV. Discussion of real cases. *Advances in Water Resources*, *24*(7), 745–762. doi: 10.1016/S0309-1708(01)00007-0

Maeght, J.-L., Rewald, B., & Pierret, A. (2013). How to study deep rootsand why it matters. *Frontiers in Plant Science*, *4*, 1–14. doi: 10.3389/fpls.2013.00299

Martínez-de la Torre, A., Blyth, E. M., & Robinson, E. L. (2019). Evaluation of Drydown Processes in Global Land Surface and Hydrological Models Using Flux. *Water*, *11*. doi: 10.3390/w11020356

Maxwell, R. M., & Condon, L. E. (2016). Connections between groundwater flow and transpiration partitioning. *Science*, *353*(6297), 377–380. doi: 10.1126/science.aaf7891

McColl, K. A., Wang, W., Peng, B., Akbar, R., Short Gianotti, D. J., Lu, H., … Entekhabi, D. (2017). Global characterization of surface soil moisture drydowns. *Geophysical Research Letters*, *44*(8), 3682–3690. doi: 10.1002/2017GL072819

Moré, J. J. (1978). The Levenberg-Marquardt algorithm: Implementation and Theory. In G. A. Watson (Ed.), *Lecture notes in mathematics* (pp. 105–116). Berlin: Springer-Verlag.

Müller, C., Waha, K., Bondeau, A., & Heinke, J. (2014). Hotspots of climate change impacts in sub-Saharan Africa and implications for adaptation and development. *Global Change Biology*, *20*(8), 2505–2517. doi: 10.1111/gcb.12586

Nash, E., & Sutcliffe, V. (1970). River flow forecasting through conceptual models Part I - A discussion of principles. *Journal of Hydrology*, *10*, 282–290. doi: 10.1016/0022-1694(70)90255-6

Nobre, A. D., Cuartas, L. A., Hodnett, M., Rennó, C. D., Rodrigues, G., Silveira, A., … Saleska, S. (2011). Height Above the Nearest Drainage - a hydrologically relevant new terrain model. *Journal of Hydrology*, *404*(1-2), 13–29. doi: 10.1016/j.jhydrol.2011.03.051

Palmer, P. I., Feng, L., Baker, D., Chevallier, F., Bösch, H., & Somkuti, P. (2019). Net carbon emissions from African biosphere dominate pan-tropical atmospheric CO2 signal. *Nature Communications*, *10*(1), 1–9. doi: 10.1038/s41467-019-11097-w

Rousseeuw, P. J., & Croux, C. (1993). Alternatives to the median absolute deviation. *Journal of the American Statistical Association*, *88*(424), 1273–1283. doi: 10.1080/01621459.1993.10476408

Rubel, F., & Kottek, M. (2010). Observed and projected climate shifts 1901-2100 depicted by world maps of the Köppen-Geiger climate classification. *Meteorologische Zeitschrift*, *19*(2), 135–141. doi: 10.1127/0941-2948/2010/0430

Schenk, H. J. (2008). The Shallowest Possible Water Extraction Profile: A Null Model for Global Root Distributions. *Vadose Zone Journal*, *7*(3), 1119. doi: 10.2136/vzj2007.0119

Schenk, H. J., & Jackson, R. B. (2002). Rooting depths, lateral root spreads and belowground aboveground allometries of plants in water limited ecosystems. *Journal of Ecology*, *90*, 480–494. doi: 10.1046/j.1365-2745.2002.00682.x

Simard, M., Pinto, N., Fisher, J. B., & Baccini, A. (2011). Mapping forest canopy height globally with spaceborne lidar. *Journal of Geophysical Research: Bio-*

geosciences, *116*(4), 1–12. doi: 10.1029/2011JG001708
Tao, S., Guo, Q., Li, C., Wang, Z., & Fang, J. (2016). Global patterns and determinants of forest canopy height. *Ecology*, *97*(12), 3265–3270. doi: 10.1002/ecy.1580
Teuling, A. J., Seneviratne, S. I., Williams, C., & Troch, P. A. (2006). Observed timescales of evapotranspiration response to soil moisture. *Geophysical Research Letters*, *33*(23), 0–4. doi: 10.1029/2006GL028178
Tian, S., Van Dijk, A. I., Tregoning, P., & Renzullo, L. J. (2019). Forecasting dryland vegetation condition months in advance through satellite data assimilation. *Nature Communications*, *10*(1), 1–7. doi: 10.1038/s41467-019-08403-x
Trigo, I. F., Dacamara, C. C., Viterbo, P., Roujean, J. L., Olesen, F., Barroso, C., … Arboleda, A. (2011). The satellite application facility for land surface analysis. *International Journal of Remote Sensing*, *32*(10), 2725–2744. doi: 10.1080/01431161003743199
Valentini, R., Arneth, A., Bombelli, A., Castaldi, S., Cazzolla Gatti, R., Chevallier, F., … Scholes, R. J. (2014). A full greenhouse gases budget of africa: Synthesis, uncertainties, and vulnerabilities. *Biogeosciences*, *11*(2), 381–407. doi: 10.5194/bg-11-381-2014
van Wijk, M. T. (2011). Understanding plant rooting patterns in semi-arid systems: An integrated model analysis of climate, soil type and plant biomass. *Global Ecology and Biogeography*, *20*(2), 331–342. doi: 10.1111/j.1466-8238.2010.00601.x
Wang-Erlandsson, L., Bastiaanssen, W. G., Gao, H., Jägermeyr, J., Senay, G. B., Van Dijk, A. I., … Savenije, H. H. (2016). Global root zone storage capacity from satellite-based evaporation. *Hydrology and Earth System Sciences*, *20*(4), 1459–1481. doi: 10.5194/hess-20-1459-2016
Weber, U., Jung, M., Reichstein, M., Beer, C., Braakhekke, M., Lehsten, V., … Ciais, P. (2009). The inter-annual variability of Africa's ecosystem productivity: a multi-model analysis. *Biogeosciences*, *6*, 285–295. doi: 10.5194/bg-6-285-2009
Williams, C. A., Hanan, N. P., Neff, J. C., Scholes, R. J., Berry, J. A., Denning, A. S., & Baker, D. F. (2007). Africa and the global carbon cycle. *Carbon Balance and Management*, *2*(1). doi: 10.1186/1750-0680-2-3
Yamazaki, D., Ikeshima, D., Sosa, J., Bates, P. D., Allen, G. H., & Pavelsky, T. M. (2019). MERIT Hydro: A High-Resolution Global Hydrography Map Based on Latest Topography Dataset. *Water Resources Research*, *55*(6), 5053–5073. doi: 10.1029/2019WR024873
Yang, Y., Donohue, R. J., & McVicar, T. R. (2016). Global estimation of effective plant rooting depth: Implications for hydrological modeling. *Water Resources Research*, *52*, 8260–8276. doi: 10.1111/j.1752-1688.1969.tb04897.x
Zeng, L., Wardlow, B. D., Xiang, D., Hu, S., & Li, D. (2020). A review of vegetation phenological metrics extraction using time-series, multispectral satellite data. *Remote Sensing of Environment*, *237*, 111511. doi: 10.1016/j.rse.2019.111511
Zhou, L., Tian, Y., Myneni, R. B., Ciais, P., Saatchi, S., Liu, Y. Y., … Hwang, T. (2014). Widespread decline of Congo rainforest greenness in the past decade. *Nature*, *508*(7498), 86–90. doi: 10.1038/nature13265